ReactorSTM : imaging catalysts under realistic conditions

Herbschleb, C.T.

Chapter 3

NO reduction on Pt(100), using the ReactorSTM Mark I

This chapter covers an investigation of the reduction of nitric oxide by carbon monoxide, on a Pt(100) model catalyst, at atmospheric pressure (1.25 bar). A combination of high-pressure scanning tunneling microscopy (Mark I) and simultaneous mass spectrometry has been used to correlate observations of the surface structure with the reaction rate and reaction mechanism. The STM images suggest that, depending on the precise composition of the reactant gas mixture, the Pt(100) surface switches between the quasi-hexagonal structure, characteristic for this surface in vacuum, and the bulklike (1x1) structure, which is 20% less dense. The reaction rates, which were observed, are interpreted in the framework of classical Langmuir-Hinshelwood kinetics, on both surface structures.

3.1 Introduction

Platinum is a good catalyst for many chemical reactions, such as CO oxidation and NO reduction. These are two of the three classes of reactions that take place in the three-way car catalyst, in which small, supported platinum, palladium, and rhodium particles are the active elements [5, 91, 92]. In this chapter, we have concentrated on NO reduction, i.e. the conversion of nitric oxide by carbon monoxide to nitrogen and carbon dioxide. Although rhodium is the main catalyst for this reaction, the (100) surface of platinum is also known to reduce NO [93, 94]. Both experimental and theoretical studies have been devoted to this reaction system. The experimental studies include temperature programmed desorption [95–97], low energy

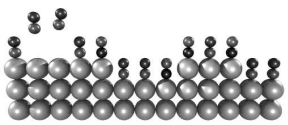

electron diffraction (LEED) [95, 98, 99], infrared reflection-adsorption spectroscopy [100], single-crystal adsorption calorimetry [99], scanning tunneling microscopy (STM) [101, 102], X-Ray photoelectron spectroscopy [103], mass spectrometry [104], molecular beam studies [97], and 3D atom probe measurements [105]. Theoretical studies include density functional theory and Monte Carlo simulations, providing various models for the active sites and the reaction mechanisms [99, 106–111].

Pt(100) can catalyze the complete conversion of NO and CO to N_2 and CO_2. The reaction is autocatalytic, and it has been proposed to be promoted by reaction intermediate species or structures like step sites [95, 101].

Clean Pt(100) exhibits a surface reconstruction, which features a quasi-hexagonal monolayer on top of the square lattice below [102, 109]. This reconstruction makes the top layer 20% denser than the unreconstructed surface. The quasi-hex reconstruction is lifted by exposing the surface to adsorbates, for instance CO, O_2, and NO, adding steps to the surface by creating adatom or vacancy islands and terrace roughness [97, 107, 114]. At low pressures, dissociation of NO only takes place on the square lattice [96] – Pt(111), which resembles the reconstructed Pt(100) surface, is not very reactive. The reaction is believed to be active above 400K; below this temperature, NO dissociation does not occur at low pressures [96, 100, 103, 107].

Most previous experiments, with surface-science techniques on the NO-CO reaction, have been performed at low pressures, since most of the employed techniques cannot tolerate high pressures. However, practical catalysts, such as the three-way catalyst, operate at high pressures, for example at and above atmospheric pressure. Recent studies on CO oxidation have revealed a strong pressure-gap effect between the traditional low pressures and the regime of atmospheric pressures. An alternative catalytic mechanism was identified at high pressures, accompanied by a significant change in the reaction rates [27, 36, 112, 113]. In the light of these observations, the present study on NO reduction by CO on Pt(100) has been performed at elevated temperature and atmospheric pressure.

3.2 Reaction Kinetics

The reduction of NO by CO is believed to proceed via Langmuir-Hinshelwood (LH) kinetics, described by the following reaction equations [93, 94, 104, 106, 108, 110].

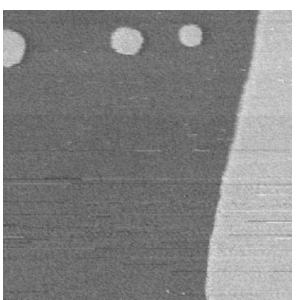

$$
\begin{array}{lll}
CO_{(g)} + * & \rightleftharpoons_{k_{-1}}^{k_1} & CO_{(ads)} \quad (1),\\
NO_{(g)} + * & \rightleftharpoons_{k_{-2}}^{k_2} & NO_{(ads)} \quad (2),\\
NO_{(ads)} + * & \rightleftharpoons_{k_{-3}}^{k_3} & N_{(ads)} + O_{(ads)} \quad (3),\\
N_{(ads)} & \rightleftharpoons_{k_{-4}}^{k_4} & \frac{1}{2}N_{2\ (g)} + * \quad (4),\\
CO_{(ads)} + O_{(ads)} & \rightleftharpoons_{k_{-5}}^{k_5} & CO_{2\ (g)} + 2* \quad (5).
\end{array}
$$

We will refer to this pathway for the formation of N_2 as pathway I. An alternative pathway (II) for the creation of N_2 is:

$$
\begin{array}{lll}
NO_{(ads)} + N_{(ads)} & \rightleftharpoons_{k_{-6}}^{k_6} & N_2O_{(ads)} + * \quad (6),\\
N_2O_{(ads)} & \rightleftharpoons_{k_{-7}}^{k_7} & N_{2\ (g)} + O_{(ads)} \quad (7),\\
N_2O_{(ads)} & \rightleftharpoons_{k_{-8}}^{k_8} & N_2O_{(g)} + * \quad (8).
\end{array}
$$

In reaction step i, k_i, and k_{-i} are the rate constants for the forward and reverse directions, respectively; a free site at the surface is indicated by $*$. For this combination of reaction steps, it is straightforward to derive the following equations for the formation rates of CO_2 and N_2 in the quasi-stationary regime[1].

$$
R_{CO_2} = k_3 \frac{k_2}{k_{-2}} \frac{p_{NO}}{\left(1 + \frac{k_1}{k_{-1}} \cdot p_{CO} + \frac{k_2}{k_{-2}} \cdot p_{NO}\right)^2}. \tag{3.2.1}
$$

$$
\begin{aligned}
R_{N_2} = \quad & \frac{k_2 p_{NO}}{4k_{-2}k_4 \left(1 + \frac{k_1}{k_{-1}} p_{CO} + \frac{k_2}{k_{-2}} p_{NO}\right)^2} \\
& \times \left[\left(\frac{1}{2} - \frac{k_8}{k_7 + k_8}\right) k_6^2 \frac{k_2}{k_{-2}} p_{NO} \right. \\
& - \left. \left(\frac{1}{2} - \frac{k_8}{k_7 + k_8}\right) k_6 \sqrt{1 + \frac{8k_4k_3k_{-2}}{k_6^2 k_2 p_{NO}}} \right] \\
& + \frac{k_3 k_2 p_{NO}}{2k_{-2} \left(1 - \frac{k_1}{k_{-1}} p_{CO} + \frac{k_2}{k_{-1}} p_{NO}\right)^2}.
\end{aligned} \tag{3.2.2}
$$

In these equations, we have made the assumptions (1) that the reaction products immediately leave the surface, thus $k_{-4} = k_{-5} = k_{-7} = k_{-8} = 0$, (2) that the coverages of N and O are negligibly small, (3) that NO and CO adsorption and desorption directly reach their equilibrium state, and (4)

[1]The derivation of R_{CO_2} and R_{N_2} according to equations 3.2.1, 3.2.2, and 3.2.3 is included in the appendix ("LH calculation") at the end of this chapter

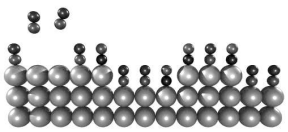

that thus the remaining reaction constants determine the overall reaction rate. The more complex structure of the formation rate for N_2 reflects the fact that it combines both pathways (reactions 4 and 7), whereas the CO_2 is only formed via pathway I (reaction 5). It is instructive to consider the N_2 formation rate in two limiting situations, namely when all N_2 is formed via the first pathway (k_4 dominant), or when all N_2 is formed via the second (k_4 negligible). In these two cases, equation 3.2.2 reduces to

$$R_{N_2} = \begin{cases} \dfrac{k_3}{2}\dfrac{k_2}{k_{-2}}\dfrac{p_{NO}}{\left(1+\frac{k_1}{k_{-1}}\cdot p_{CO}+\frac{k_2}{k_{-2}}\cdot p_{NO}\right)^2} & k_4 \text{ dominant} \\ \dfrac{k_3 k_8}{k_7+k_8}\dfrac{k_2}{k_{-2}}\dfrac{p_{NO}}{\left(1+\frac{k_1}{k_{-1}}\cdot p_{CO}+\frac{k_2}{k_{-2}}\cdot p_{NO}\right)^2} & k_4 \text{ negligible.} \end{cases} \tag{3.2.3}$$

Interestingly, in each of these two limiting situations, the N_2 formation rate varies with the partial pressures of NO and CO, in precisely the same way, identical to the dependence of the formation rate of CO_2 on these partial pressures. Combining the relevant reaction rate constants in three parameters K_i ($i = 1..3$), equations 3.2.3 and 3.2.1 can be rewritten, giving

$$R_{N_2}, R_{CO_2} = K_1^{N_2,CO_2}\frac{p_{NO}}{\left(1+K_2\cdot p_{CO}+K_3\cdot p_{NO}\right)^2}. \tag{3.2.4}$$

For reaction pathway I, $K_1^{N_2} = \frac{k_3 k_2}{2k_{-2}} = \frac{1}{2}K_1^{CO_2}$. For reaction pathway II, $K_1^{N_2} = \frac{k_3 k_8 k_2}{(k_7+k_8)k_{-2}}$, and $K_1^{CO_2} = \frac{k_3 k_2}{k_{-2}}$ (the same as for pathway I). This means that $K_1^{N_2}$ and $K_1^{CO_2}$ depend, in all cases, directly on the NO dissociation rate (k_3), and on the reaction constant $\frac{k_2}{k_{-2}}$, for NO adsorption/desorption. In the case of pathway II, $K_1^{N_2}$ is also determined by the ratio between the rate constants for N_2 and N_2O formation, via the factor $\frac{k_8}{k_7+k_8}$. The only difference between $K_1^{N_2}$ for the N_2 formation rates at high and low k_4 is a mere factor $\frac{2k_8}{k_7+k_8}$. For intermediate k_4-values, we have been forced to return to the more complex form of equation 3.2.2. In all cases, $K_2 = \frac{k_1}{k_{-1}}$ is the reaction constant for CO adsorption/desorption, and $K_3 = \frac{k_2}{k_{-2}}$ is the reaction constant for NO adsorption/desorption.

Since the form of the equations, for R_{N_2} for both pathways and R_{CO_2}, are the same, this form will be used later, in an attempt to fit the experimental N_2 and CO_2 formation rates, using the K_i's as fitting parameters. As mentioned, the formation rate for CO_2 is double the first N_2 formation rate

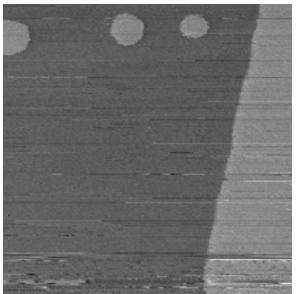

of equation 3.2.3, so that, if the N_2 formation rate is dominated by the first pathway, $R_{CO_2} = 2R_{N_2}$.

We close this section by noting that a more complete description of the set of reaction rates might require the introduction of non-linear elements in one or more reaction rates, since at low pressures, bi-stability and oscillations have been observed [97–99, 111, 115].

3.3 The Pt(100) sample

In this work, a platinum single crystal, cut and polished with the (100) surface orientation, was used. It was prepared in the UHV chamber by multiple cycles of (1) argon ion sputtering, at an ion energy of 600 eV, (2) annealing in a $1 \cdot 10^{-6}$ mbar oxygen atmosphere at 1000 K, and (3) flash annealing to a somewhat higher temperature in UHV. Low energy electron diffraction (LEED), in combination with Auger electron spectroscopy, was used to verify the crystalline quality and the cleanliness of the sample surface, prior to transferring it to the ReactorSTM. A typical LEED pattern is shown in figure 3.1 A.

Pt(100) reconstructs into a 20% denser quasi-hexagonal lattice, with reported overlayer periodicities of (1x5), (5x20) and (5x25) rotated 0.7° with respect to the underlying lattice [116, 117, 121]. This can generally be written in matrix form as $\left(\begin{smallmatrix} N & 1 \\ -1 & 5 \end{smallmatrix}\right)$. A ball model of this structure is depicted in figure 3.1 B. Because the symmetry of the quasi-hexagonal overlayer is different from the symmetry of the square lattice below, a Moiré pattern is obtained, when imaging the reconstructed surface. Figure 3.1 C shows a 50.1 nm x 50.1 nm STM image exhibiting this Moiré pattern clearly, from which we can determine the commensurate unit cell. The unit cell is defined by the rectangle (d_1, d_2), which includes two lines of the Moiré pattern in the direction of d_1. The reason for this can be seen in figure 3.1 D: every second segment along d_1, in between two pattern lines d_2, has a broader appearance in the STM image, so in order for the unit cell to be commensurate, we have to include $2d_1$. To determine the number of platinum atoms n_i along d_i, we count the number of lines N_i along a distance D_i, for $i = 1, 2$, and use the equation $n_i = D_i/(N_i d_{Pt,i})$, in which $d_{Pt,i}$ is the distance between the platinum atoms. For direction d_1, the inter platinum distance corresponds to the bulk distance, which is 2.77 Å [118]. For direction d_2, we have to take the hexagonal packing into account, which leads to $d_{Pt,2} = 0.5\sqrt{3} \cdot 2.77 = 2.40$ Å. Doing the exercise, a periodicity of (4x25) for the commensurate unit cell

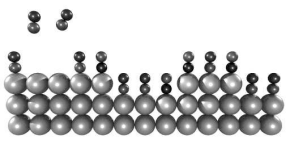

was obtained, coinciding well with the literature.

Figure 3.1 E shows a height profile of image C along the line (B), exhibiting a (monatomic) step height on Pt(100) of 2 Å. This coincides with the reported monatomic step height on Pt(100) [121]. Furthermore, figure 3.1 F shows an STM image in which atomic row resolution on the clean Pt(100) crystal was obtained. A row distance of 5.1 Å, which corresponds to twice the distance between the hexagonal packed rows, has been found. Atomically resolved STM images, obtained under UHV conditions, have shown that every second atomic row along this direction appears higher than its neighboring rows [120]; this indicates that only the higher rows were imaged with the ReactorSTM.

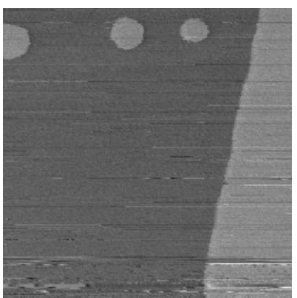

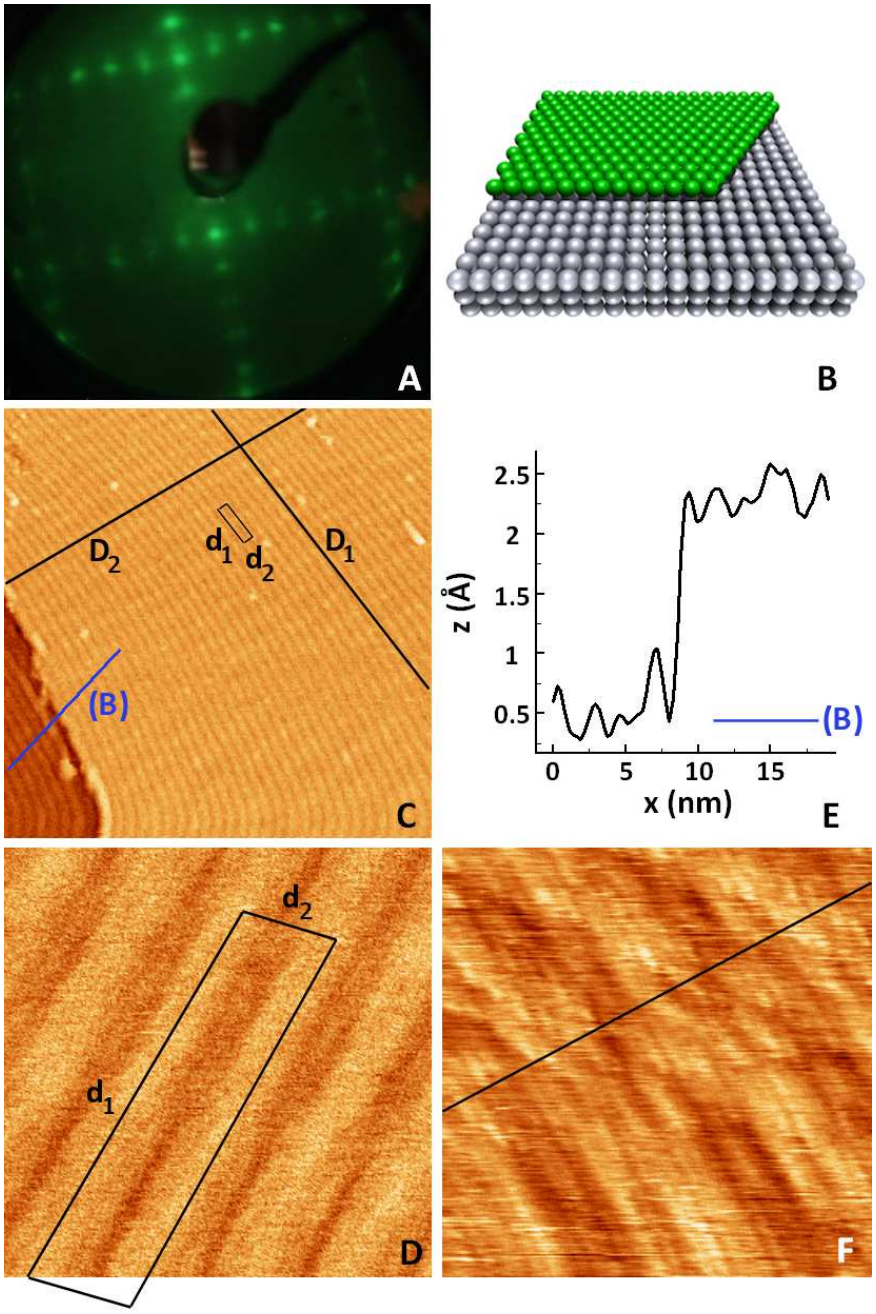

Figure 3.1: (A) A typical LEED pattern for clean Pt(100). Due to the incommensurate overlayer, with respect to the bulk, the spots are split. (B) A ball model of the reconstructed Pt(100) surface showing the quasi-hexagonal overlayer on the square lattice below. (C) A 50.1 x 50.1 nm^2 STM image of the reconstructed Pt(100) surface. (D) A 5.5 x 5.5 nm^2 STM image, indicating the unit cell of the quasi-hexagonal overlayer (d_1, d_2), also indicated in image C. (E) The height profile of line (B) in image C, showing a step height of 2 Å on Pt(100). (F) A 5.5 x 5.5 nm^2 STM image of Pt(100), on which we obtained atomic row resolution on the reconstructed Pt(100) surface. For all STM images shown here, $V_b = -100$ mV, and $I_t = 0.2$ nA.

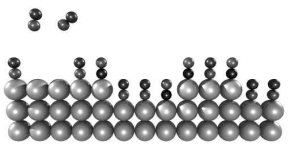

3.4 Results & Discussion

3.4.1 STM images

In this section, STM images taken by the ReactorSTM Mark I in different NO/CO partial pressure ratios, at elevated temperatures, are presented. Figures 3.2 and 3.3 show STM images obtained at 382 K and 395 K, in combination with the gas compositions to which the surface was exposed. The numbers in the partial-pressure graphs refer to the corresponding STM images. Image A, in figure 3.2, is an overview of the surface when it has been exposed to an NO-rich environment at 382 K, a few minutes after having been in a CO-rich mixture. The switch to the high partial pressure of NO has resulted in a high density of vacancy islands on the originally flat surface. The vacancy islands have a depth corresponding to the monatomic step height of platinum, 2.0 Å [112, 119]. Images B, C, & D are three consecutive images, zoomed in on the area indicated by the black square in image A. They demonstrate the high surface mobility; the vacancy islands disappear, and the wavy terrace edges straighten. Image E has been zoomed out again, and shows that the surface recovery has also taken place on a larger scale. Image A, in figure 3.3, is the flat surface in an NO-rich environment at 395 K. Image B was recorded during the switch to a CO-rich environment. As can be recognized in images B and C, the surface roughened, under these conditions, by the introduction of adatom islands, and waviness in the terrace edges. Minutes later, the roughness was observed to decay, as can be seen in images D and E.

The changes in the STM images can be interpreted in terms of a surface phase transition between NO-rich and CO-rich conditions. We propose that the surface is reconstructed into the quasi-hexagonal termination, when exposed to the NO-rich mixture, whereas the surface reconstruction is lifted to the (1x1) periodicity, when the mixture is switched to CO-rich. There are four pieces of evidence in support of this interpretation. Firstly, the structure observed under NO-rich conditions differs from a surface oxide. The height differences in the images all occur as steps, with the regular monatomic step height of metallic platinum, as shown in images A and B, and the height profiles D_1 to D_3, in part I of figure 3.4. For comparison, in image C, we also show an image of the same surface, with an oxygen-induced surface oxide. This was observed in a separate experiment, where we saw that oxidation makes the surface much rougher, and the height variations are not quantized in units of the metallic step height. Secondly, the quasi-hex surface termination is more dense than the (1x1) lattice, implying that reconstructing the

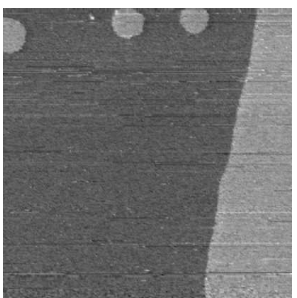

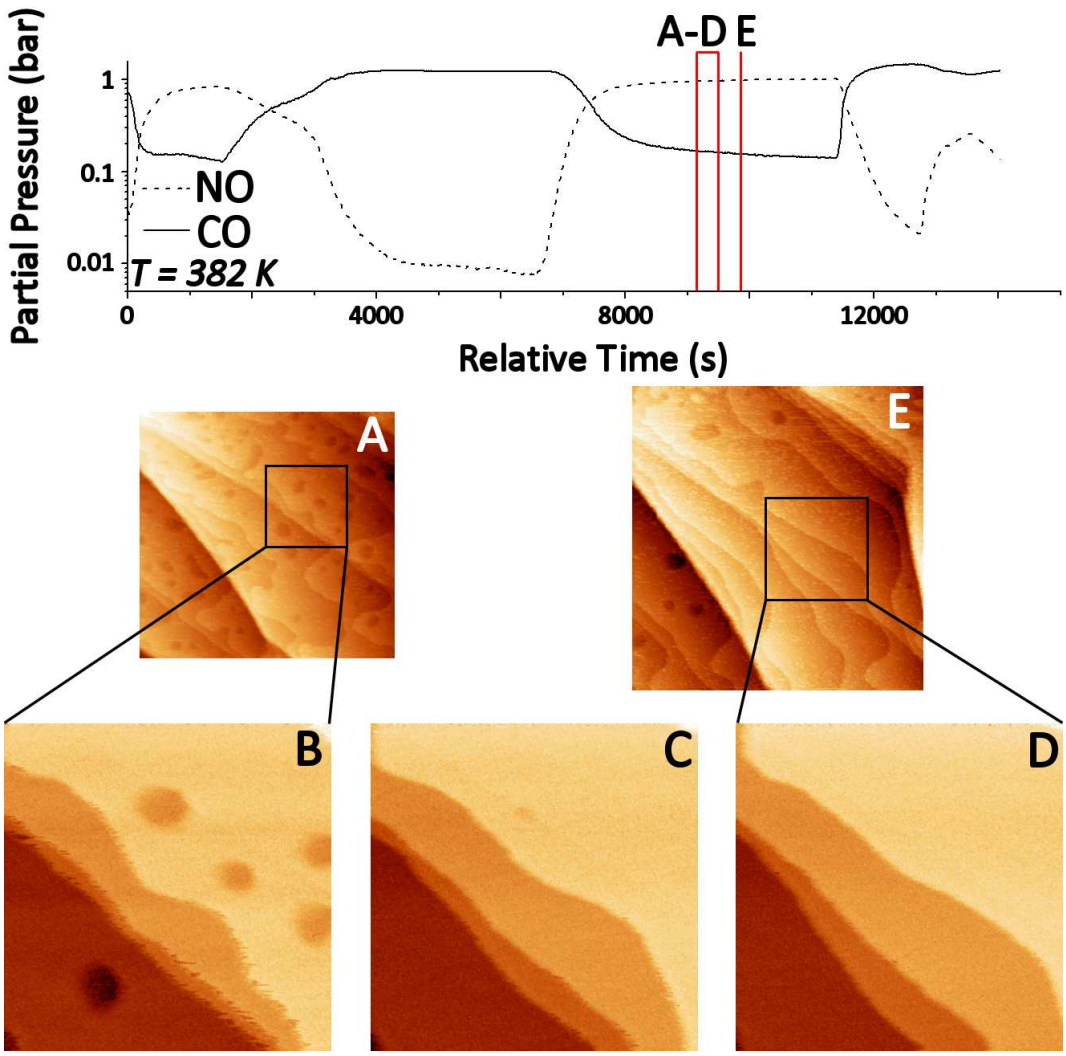

Figure 3.2: The gas compositions and STM images of Pt(100), in a flowing mixture of NO/CO, at a total pressure of 1.25 bar at 382 K; V_{bias} = 0.08 V; I_{tunnel} = 0.2 nA. A: 310 x 300 nm^2; B to D: 120 nm^2; E: 350 x 370 nm^2.

surface, starting from the unreconstructed surface, should yield vacancy islands. This is what has indeed been observed systematically, for example in figure 3.2. Similarly, de-reconstructing the surface, from quasi-hex to (1x1), should yield adatom islands, again in accordance with repeated STM observations. In both cases, after the phase transition occurred, we observed that surface diffusion slowly reduced the roughness. This shows that the observed roughness does not reflect the equilibrium structure, neither under NO-rich nor CO-rich conditions; rather, it should be regarded as a temporary, i.e.

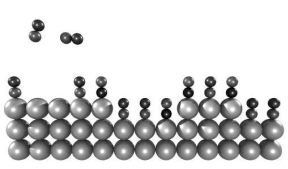

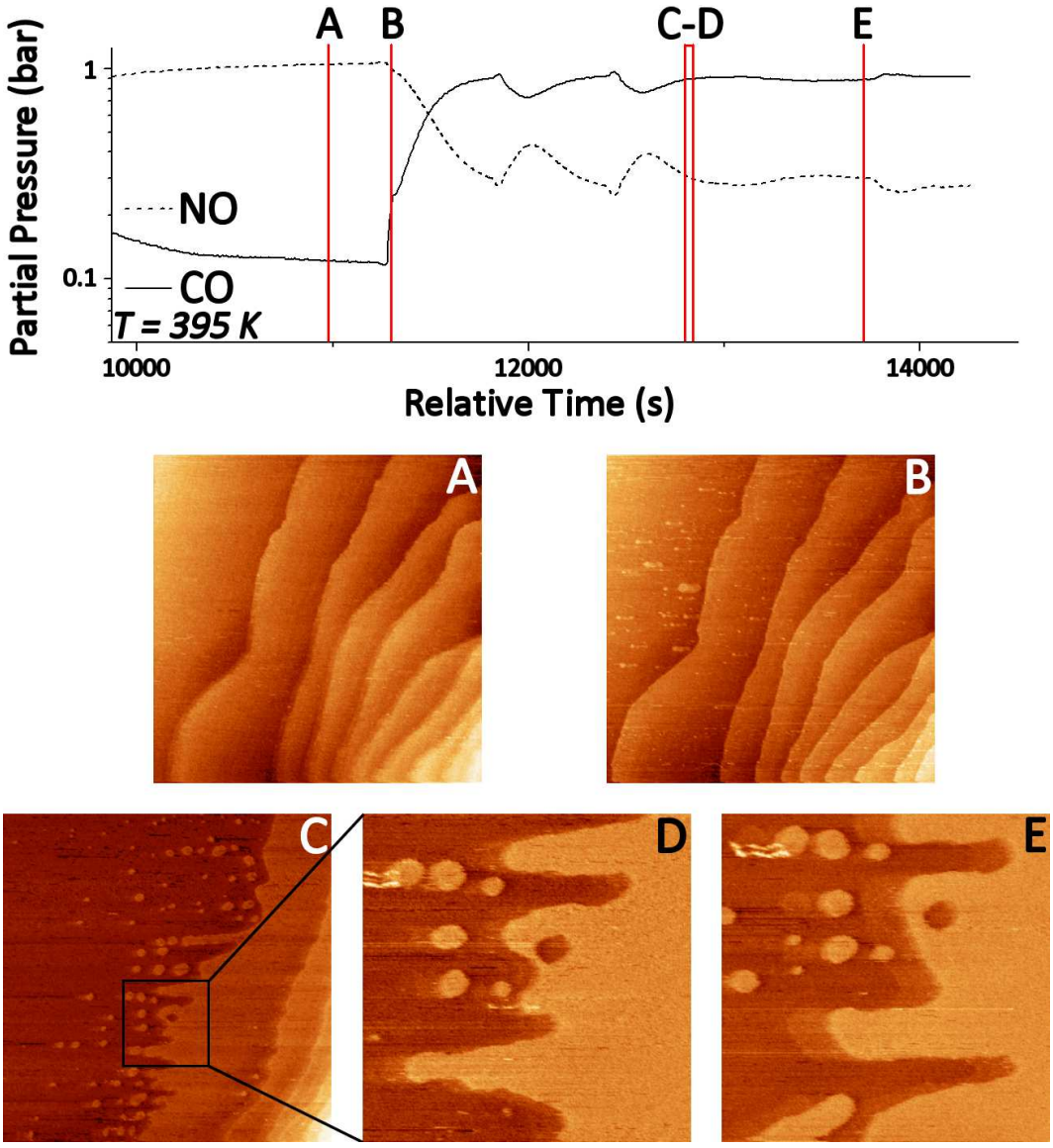

Figure 3.3: The gas compositions and STM images of Pt(100), in a flowing mixture of NO/CO, at a total pressure of 1.25 bar at 395 K; V_{bias} = 0.08 V; I_{tunnel} = 0.2 nA. A, B, C: 400 nm^2; D, E: 120 nm^2.

non-equilibrium structure, necessary to accommodate a surface density mismatch of the Pt atoms between the two structures. Thirdly, we observed that the surface temporarily responded significantly to its interaction with the STM tip, when the gas composition switched from NO-rich to CO-rich. This is demonstrated in part II of figure 3.4. Image E shows the Pt(100)

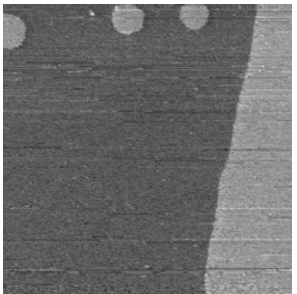

surface, just after the switch to a CO-rich mixture. As discussed before, the switch in gas composition leads to the formation of adatom islands. In the consecutive images, such as image F of figure 3.4, the tip is observed to drag material over the surface, which is evidenced by the alignment of the adatom islands and the terrace roughness along the scanning direction of the STM tip (this is the horizontal direction in all images). We believe this to be the consequence of the presence of a high density of mobile adatoms and small adatom islands, generated by the quasi-hex to (1x1) transition. This situation is temporary – after a few minutes, the surface no longer responds to the tip, while the adatom structures and the step roughness slowly decay, as can be seen in the lower part of figure 3.2. The final piece of evidence for the quasi-hex to (1x1) transition is the observation, in part III of figure 3.4, that the adatom and vacancy islands exhibit a weak hexagonal symmetry in NO-rich atmospheres, as shown in images G and H, whereas the vacancy islands, observed under CO-rich conditions, exhibit a weak square symmetry, as shown in image I. Our proposal of Pt(100) reconstructing in an NO-rich environment is at variance with earlier research on this reaction system, in which NO is lifting the reconstruction rather than stabilizing it [97, 119]. This difference is attributed to the fact that the surface was exposed to a high (ambient) pressure of NO, instead of a more traditional, low pressure of e.g. 10^{-6} mbar. In other words, this difference should be regarded as a *pressure gap* effect.

Since the surface density of the quasi-hex lattice is 20% higher than that of the (1x1) substrate lattice of Pt(100), we should expect the area of vacancy or adatom islands, created upon switching gas composition, to be 20% of the total area. Although our STM images are certainly consistent with this, the quality of many of our images is not sufficiently good to quantify the relative adatom or vacancy island coverage accurately. Another complicating factor is the role of the steps, which can easily accommodate adatoms or vacancies, and can therefore locally reduce their numbers. Furthermore, as observed in our images, surface diffusion was efficient in quickly removing the height variations, which made only the very first images, immediately after the switching, have the full adatom or vacancy island density. Unfortunately, the characteristic moiré pattern of the hex-reconstructed Pt(100) surface [121], which we observe under room temperature and vacuum conditions, could not be resolved in NO-rich atmospheres, probably due to the NO-induced loss of image resolution.

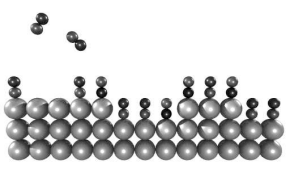

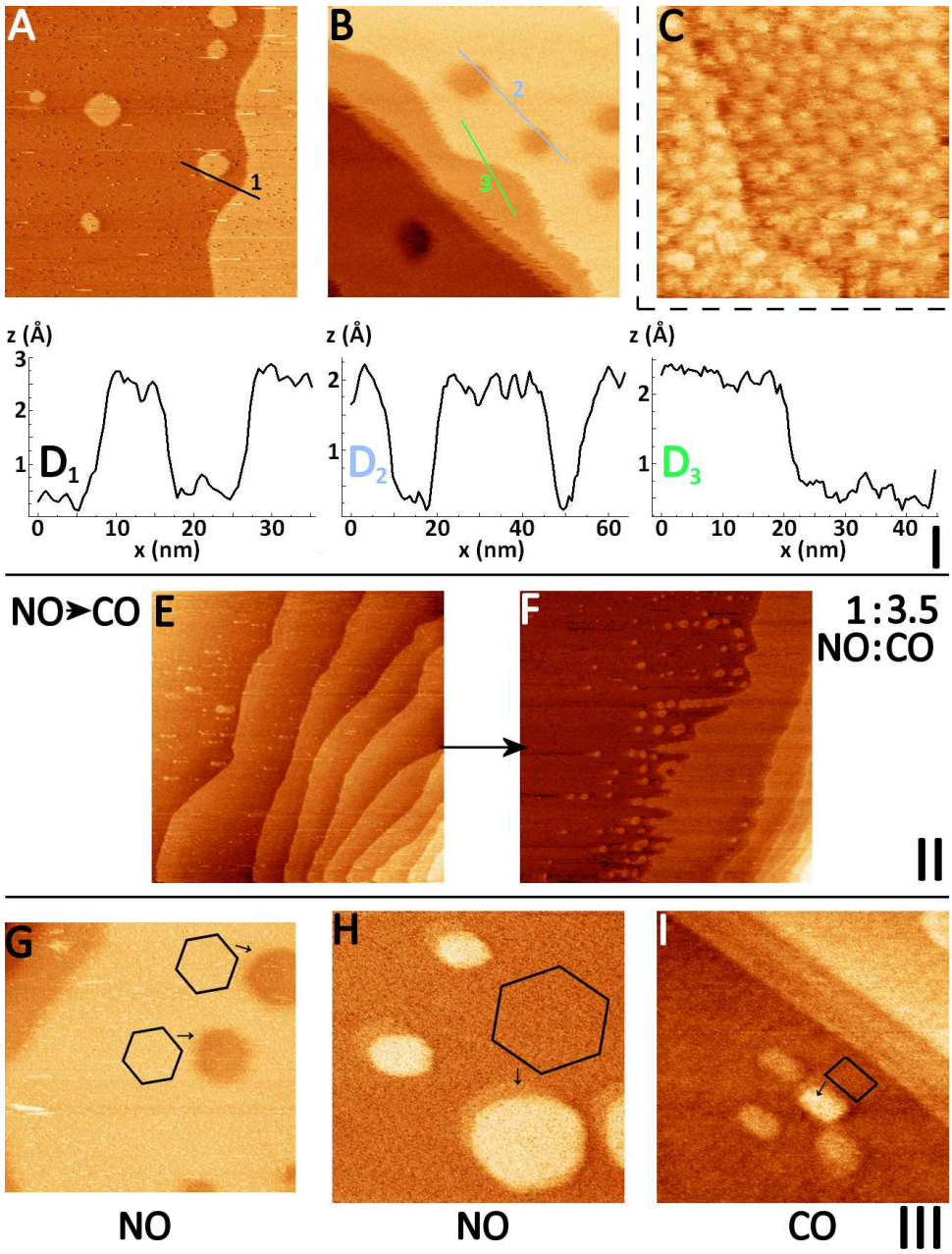

Figure 3.4: Part I: Images A and B were taken in an NO-rich flow. The lines labelled 1,2, and 3 refer to the three height profiles in D_1 to D_3, each showing height differences corresponding to the step height of Pt(100). For comparison, image C shows the roughness on this surface when it is oxidized in an O_2-rich flow. Part II: Two images illustrating the high surface mobility induced by the STM tip immediately after switching from an NO-rich to a CO-rich gas composition. Part III: STM images indicating weak hexagonal and square symmetries of vacancy and adatom islands in NO-rich and CO-rich environments, respectively.

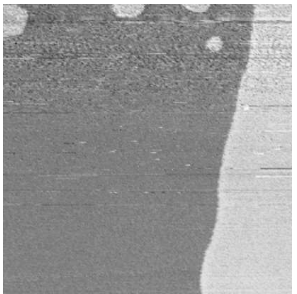

3.4.2 Interpretation of QMS signals

Since CO and N_2 have the same molecular mass, 28 amu, the mass spectrometer cannot distinguish between the two directly. In order to obtain the partial pressure of the N_2 that was produced in the reaction, we combined the convoluted signal S_{28}, at mass 28, with the signal S_{12} for atomic carbon (^{12}C), which is directly proportional to the partial pressure of CO.

$$p_{N_2} = c \cdot [S_{28} \; - \; n \cdot S_{12} \; - \; m \cdot S_{30}]. \tag{3.4.1}$$

Here, c is a calibration factor, relating the QMS signals to actual pressures. The factor n is a normalization constant, which corrects for the sensitivity ratio between the signals, at masses 28 and 12, to the partial pressure of CO. This factor was determined to be $n = 1.23$, from measurements under CO-rich conditions, when the formation rate of N_2 was negligible. Equation 3.4.1 also contains a term to correct for the contamination of the NO gas, used in the experiment, by a trace amount of $m = 5 \cdot 10^{-4}$ of N_2. This contribution scales with the signal S_{30} of NO.

3.4.3 Kinetics

In this section, the reaction kinetics, as measured with the QMS during the acquisition of the STM images, will be scrutinized. As concluded in the previous section, the surface exhibits either a hexagonal or a square structure, depending on the ratio between the partial pressures of NO and CO. These structures are thought to be two different terminations of the metal crystal, each with its own configuration of adsorbed species. Since the surface contains no special, reacted materials, such as a platinum oxide layer, we do not expect special reaction mechanisms, such as the Mars-van-Krevelen mechanism [27]. It has been assumed that the reactions simply proceed according to LH-kinetics, under both NO-rich and CO-rich conditions. In this section, therefore, the equations derived in section 3.2 for the formation rates of N_2 and CO_2 have been used, in an attempt to fit the measured partial pressures for both cases. It must be emphasized that the quasi-hexagonal structure and the square (1x1) structure differ significantly, both in atomic density and in geometry and symmetry. This should have an effect on the bonding geometries, and the corresponding binding energies, for the reactant and product molecules on the surface, and for reaction energy barriers. Such differences should be accompanied by differences in the kinetic parameters in the rate equations, for both situations. Before introducing separate values for the kinetic parameters for NO-rich and CO-rich conditions, we will first

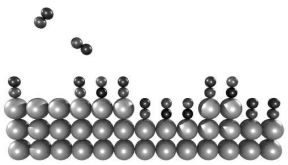

attempt to fit the measurements with a single set of parameter values.

In figure 3.5, the top graph shows the CO/NO compositions, to which the surface was exposed, and the production of N_2 and CO_2 measured at each stage. The signatures of LH-kinetics are clearly visible in the reaction rates. The reaction rates are low in both CO- and NO-rich atmospheres, and they maximize for intermediate mixtures.

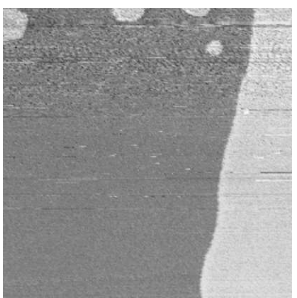

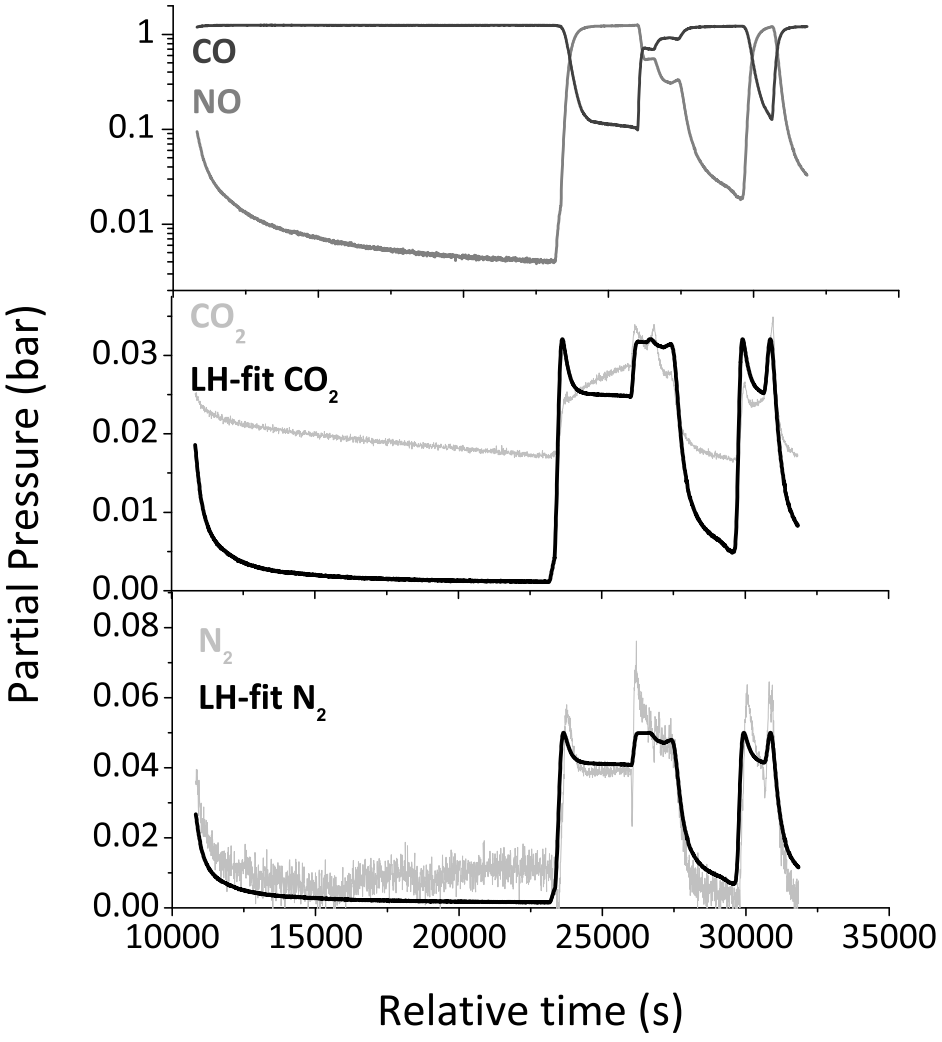

Figure 3.5: The reaction rates, (partial pressures), for N_2 and CO_2 production for the reactant gas mixtures, shown in the upper panel. The experimental partial pressures are indicated by the red curve, for CO_2, in the middle panel, and by the blue curve, for N_2, in the lower panel. The black curves in the lower two panels are the best-fit calculations, discussed in the text.

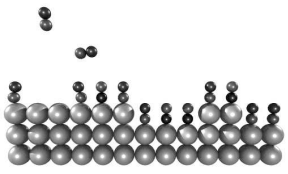

In section 3.2, it has been shown that the rate constants for the individual reaction steps combine into three fitting parameters K_i (equation 3.2.4). Table 3.1 shows two sets of optimal values, which were determined for these parameters by a least squares fitting procedure [122], either to the N_2 data or to the CO_2 data in figure 3.5.

Table 3.1: The optimal values for the parameters K_i, obtained separately by fitting equation 3.2.4 and its analog for CO_2 to the measured rates of N_2 and CO_2 formation, in figure 3.5.

	$K_1^{N_2,CO_2}\left[\frac{cm^2}{bar\cdot s}\right]$	$K_2\left[\frac{1}{bar}\right]$	$K_3\left[\frac{1}{bar}\right]$
N_2	0.40 ± 0.07	0.01 ± 0.01	1.95 ± 0.15
CO_2	0.29 ± 0.02	0.01 ± 0.01	2.3 ± 0.2

Before discussing the fits in detail, the values of the fitting parameters will be briefly addressed. It is clear that K_2 and K_3 have the same optimal values, when fitting either N_2 or CO_2. This is in full accordance with our expectations from section 3.2. The ratio between the K_1 values for the CO_2 fit and the N_2 fit is 0.7. This is much lower than the value of 2, expected when the reaction would have been dominated completely by reaction pathway I, for which $R_{CO_2} = 2R_{N_2}$. We further note that K_2 is very low, indicating that CO has a relatively strong tendency to desorb, in this reaction system. By contrast, K_3, which compares the adsorption and desorption rate constants of NO, is in the order of unity.

The LH-curves, in the middle and lower panels of figure 3.5, provide reasonable fits to the measured signals. The typical LH features, such as the reaction peaks when the mixture is changing from CO-rich to NO-rich and vice versa, and also the variations of the reaction rates during more modest changes in the composition of the reactant mixture, are all reproduced, at least qualitatively, by the fits. The fit to the CO_2 signal is not as good as that for the N_2 signal. As concluded above, from the ratio between the K_1 values, N_2 production is not fully dominated by the first pathway, implying that also N_2O has also been produced. Unfortunately, the mass of N_2O, 44 amu, is equal to that of CO_2, so that their peaks in the mass spectrum add up. It should be further noted that the extreme sharpness of the peaks, in the measured N_2 signal, is not represented by the fit. This discrepancy might be explained in two ways; firstly, the mass sweep of the QMS introduced systematic small differences between the precise readout times of the individual

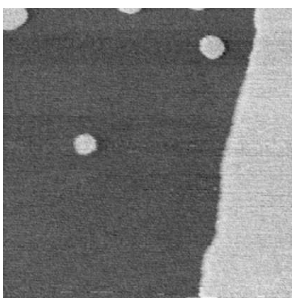

mass signals. When rapid changes occur in the partial pressures of the gasses involved in the reaction system, this may lead to a noticeable, transient error, when different signals are subtracted from each other, following equation 3.4.1. Secondly, as we will discuss now, the description of the reaction rates, in terms of a single set of kinetic parameters, may be inadequate, in view of the occurrence of two distinct surface structures.

In section 3.4.1, it was argued that the sudden introduction or sudden lifting of the quasi-hexagonal surface reconstruction of Pt(100) has been the cause of the surface roughness and the change in symmetry (hexagonal versus square), which were introduced by changing from NO-rich to CO-rich gas mixtures, and vice versa. Accompanying the difference between the two surface structures, we should also expect a difference in the kinetics of the NO reduction reaction. In the fits, in figure 3.5, this has been completely ignored. The fact that the calculations, in this figure, nevertheless qualitatively fit the observations, indicates that the reaction mechanism does not change. Thus the reaction rates should be described by Langmuir-Hinshelwood kinetics for both structures, and the values for the rate constants should be quite similar. The comparison between calculated and measured reaction rates will now be refined, by separating the measurements into two different regimes, one corresponding to the data for which the STM observations indicate the surface to be reconstructed, and the other corresponding to the unreconstructed surface. The STM images show that the two regimes correspond approximately to $p_{NO} > p_{CO}$ and $p_{NO} < p_{CO}$, respectively. For each of these two regimes, a separate set of values for the three parameters for the LH-kinetics was determined.

$$R_{N_2} = \begin{cases} K_1^{hex} \dfrac{p_{NO}}{\left(1 + K_2^{hex} p_{CO} + K_3^{hex} p_{NO}\right)^2} & p_{NO} > p_{CO} \\ K_1^{(1x1)} \dfrac{p_{NO}}{\left(1 + K_2^{(1x1)} p_{CO} + K_3^{(1x1)} p_{NO}\right)^2} & p_{NO} < p_{CO}, \end{cases} \tag{3.4.2}$$

where parameters K_i^{hex} define the fit for the reconstructed surface, and $K_i^{(1x1)}$ that for the unreconstructed surface. The result of this procedure is shown in the lower panel of figure 3.6; for comparison, the upper panel repeats the best fit to the N_2 signal for the 'single-kinetics' model, which was already shown in figure 3.5. The introduction of the three additional parameters has clearly led to a modest improvement of the fit. In particular,

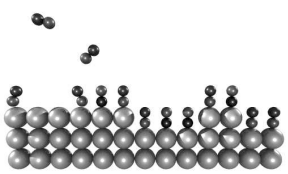

the CO-rich episodes are better described, even though the match between calculation and measurement is still not ideal.

The best-fit values for the six parameters of the 'dual-kinetics' model are listed in table 3.2, together with the three values for the 'single-kinetics' fit.

Table 3.2: The optimal values of the fitting parameters for the N_2 reaction rate for the 'single-kinetics' fit (figure 3.5), and for the 'dual-kinetics' fit (figure 3.6). The units of the parameters are the same as in table 3.1. The right column shows the goodness of fit, expressed as the normalized χ^2_ν, defined in equation 3.4.2.

Single kinetics	$K_1^{N_2}$	K_2	K_3	χ^2_ν
	0.40 ± 0.07	0.01 ± 0.01	1.95 ± 0.15	8.9
Dual kinetics	K_1^{hex}	K_2^{hex}	K_3^{hex}	χ^2_ν
hex	0.43 ± 0.05	0.01 ± 0.01	2.10 ± 0.20	
				9.1
	$K_1^{(1x1)}$	$K_2^{(1x1)}$	$K_3^{(1x1)}$	
(1x1)	0.33 ± 0.03	0.01 ± 0.01	1.60 ± 0.10	

In order to compare the quality of the fits on a more quantitative basis, the normalized χ^2_ν [123] for both fits has been determined.

$$\chi^2_\nu = \frac{1}{N-\nu-1} \sum_{i=0}^{N} \frac{(F_i - D_i)^2}{F_i}, \tag{3.4.3}$$

in which N is the number of data points, ν the number of fitting parameters (either 3 or 6), and F_i, and D_i are the theoretical and measured values of the reaction rate at point i. As the right column of table 3.2 shows, the difference between the goodness-of-fit values for the two models is statistically insignificant, mainly due to the remaining, systematic discrepancy between the measured N_2 production rates and both models. In principle, a similar, dual-kinetics fitting procedure can be carried out for the CO_2 signal, but the quality of the fit to this signal has been relatively poor. Possibly, a full fitting procedure, involving all 16 reaction rate constants, could lead to a fit with a χ^2_ν value closer to unity.

From figure 3.6 and table 3.2, the following information has been extracted. The dual-kinetics fit for the quasi-hexagonal episodes, in NO-rich

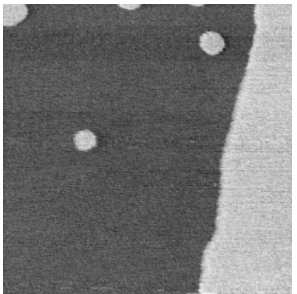

mixtures, is very close to the single-kinetics fit, which is also reflected in rather similar values of the three fitting parameters for the quasi-hexagonal structure, and for the single-kinetics model. On the other hand, as already indicated, the fit for the square (1x1) episodes, under CO-rich conditions, is clearly different from, i.e. better than, the single-kinetics fit. Indeed, two of the three parameters assume somewhat different values in this case. The biggest difference can be found in K_3, the ratio between the rate constants for adsorption and desorption of NO, which is always high, but tends more strongly towards NO adsorption in the quasi-hexagonal phase than in the square phase. K_1 is somewhat lower in the square phase than in the quasi-hexagonal phase, which means that, either the NO dissociation step is more difficult, or the N_2O production is higher, in this phase.

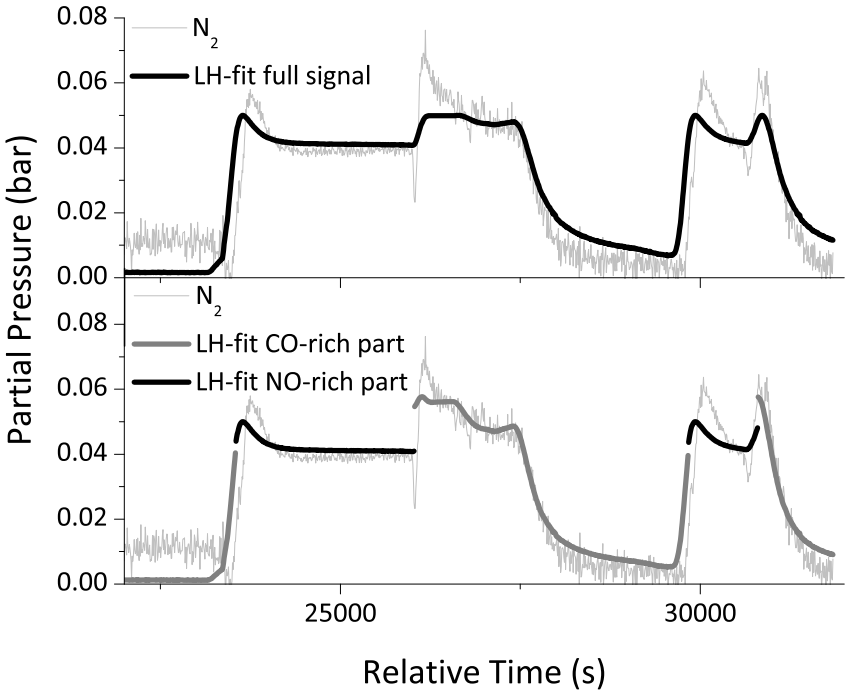

Figure 3.6: (Lower panel) The fit obtained according to the dual-kinetics Langmuir-Hinshelwood model for the production of N_2, compared with the experimental N_2 signal. (Upper panel) For reference, the upper panel repeats the single-kinetics fit of figure 3.5.

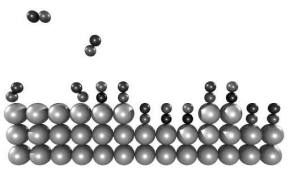

3.5 Conclusions

In this chapter, the reduction of NO by CO on the Pt(100) surface, by in-situ STM, at atmospheric pressures and elevated temperatures, combined with simultaneous mass spectrometry has been investigated. The STM images indicate that, depending on the CO:NO ratio, the surface switches between two different structures, with either a square or a hexagonal symmetry, reflecting the unreconstructed (1x1) surface and the quasi-hexagonally reconstructed Pt(100) surface, respectively. The measured rates of N_2 and CO_2 production in terms of Langmuir-Hinshelwood kinetics has been analyzed. In this procedure, the possibility of two separate LH regimes, namely one for the (1x1) surface, and the other for the quasi-hexagonal structure have been considered. Even though the latter, dual-kinetics, fit follows the measurements more closely, the systematic differences between measurements and models are too severe to quantify this improvement.

Appendix: LH calculation

In this appendix, the derivation of R_{CO_2} and R_{N_2} is shown, using the assumptions, as listed in section 3.2. Let us start with rewriting the reaction equations with corresponding reaction constants k_i:

$$
\begin{array}{lll}
CO_{(g)} + * & \rightleftharpoons_{k_{-1}}^{k_1} & CO_{(ads)} \quad (1),\\
NO_{(g)} + * & \rightleftharpoons_{k_{-2}}^{k_2} & NO_{(ads)} \quad (2),\\
NO_{(ads)} + * & \rightleftharpoons_{k_{-3}}^{k_3} & N_{(ads)} + O_{(ads)} \quad (3),\\
N_{(ads)} & \rightleftharpoons_{k_{-4}}^{k_4} & \frac{1}{2}N_{2\ (g)} + * \quad (4),\\
CO_{(ads)} + O_{(ads)} & \rightleftharpoons_{k_{-5}}^{k_5} & CO_{2\ (g)} + 2* \quad (5),\\
NO_{(ads)} + N_{(ads)} & \rightleftharpoons_{k_{-6}}^{k_6} & N_2O_{(ads)} + * \quad (6),\\
N_2O_{(ads)} & \rightleftharpoons_{k_{-7}}^{k_7} & N_{2\ (g)} + O_{(ads)} \quad (7),\\
N_2O_{(ads)} & \rightleftharpoons_{k_{-8}}^{k_8} & N_2O_{(g)} + * \quad (8).
\end{array}
$$

In the steady state approximation, we can directly define the reaction rate for the formation of CO_2 and N_2 from the equilibrium coverage ϑ_i, of the species on the surface.

$$\frac{d\vartheta_{CO_2}}{dt} \equiv R_{CO_2} = k_5\vartheta_{CO}\vartheta_O. \tag{3.5.1}$$

$$\frac{d\vartheta_{N_2}}{dt} \equiv R_{N_2} = k_4\vartheta_N^2 + k_8\vartheta_{N_2O}. \tag{3.5.2}$$

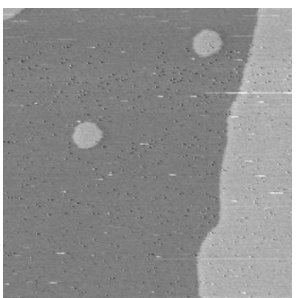

In order to be able to fit Langmuir-Hinshelwood kinetics to the data, obtained by the QMS, which comes in the form of partial pressures of reactants and reaction products, the expressions 3.5.1 and 3.5.2 need to be rewritten, as a function of the partial pressures of the reactants CO and NO. Let's start with the derivation of R_{CO_2}, which can be rewritten as a function of ϑ_{CO} and ϑ_{NO}, via the coverage of oxygen atoms on the surface, ϑ_O,

$$\frac{d\vartheta_O}{dt} = k_3\vartheta_{NO}(1-\vartheta_{NO}-\vartheta_{CO}) - k_5\vartheta_{CO}\vartheta_O = 0$$

$$\Leftrightarrow R_{CO_2} = k_3\vartheta_{NO}(1-\vartheta_{CO}-\vartheta_{NO}). \tag{3.5.3}$$

ϑ_{CO} and ϑ_{NO} now need to be written as functions of the reactant pressures p_CO and p_NO. We will start by writing down the steady state situation, from the reaction equations,

$$\frac{d\vartheta_{CO}}{dt} = k_1 p_{CO}(1-\vartheta_{CO}-\vartheta_{NO}) - k_{-1}\vartheta_{CO} = 0$$

$$\frac{d\vartheta_{NO}}{dt} = k_2 p_{NO}(1-\vartheta_{CO}-\vartheta_{NO}) - k_{-2}\vartheta_{NO} = 0.$$

These can be substituted into each other to obtain functions of the coverages, solely as a function of the reactant pressures, after which the result can then be substituted into equation 3.5.3, to obtain the reaction rate for the formation of CO_2:

$$\vartheta_{CO} = \frac{\frac{k_1}{k_{-1}}p_{CO}}{1+\frac{k_1}{k_{-1}}p_{CO}+\frac{k_2}{k_{-2}}p_{NO}} \tag{3.5.4}$$

$$\vartheta_{NO} = \frac{\frac{k_2}{k_{-2}}p_{NO}}{1+\frac{k_1}{k_{-1}}p_{CO}+\frac{k_2}{k_{-2}}p_{NO}} \tag{3.5.5}$$

$$\Rightarrow R_{CO_2} = k_3\frac{\frac{k_2}{k_{-2}}\cdot p_{NO}}{\left(1+\frac{k_1}{k_{-1}}\cdot p_{CO}+\frac{k_2}{k_{-2}}\cdot p_{NO}\right)^2}. \tag{3.5.6}$$

The derivation, to obtain the expression for the reaction rate for N_2 formation, is slightly more complicated. Again, the coverages of the various species, on the surface on which the N_2 reaction rate depends, should be rewritten, by reactant pressures. Looking at equation 3.5.1, the steady state situations for ϑ_N and ϑ_{N_2O} first need to be written down, which yields

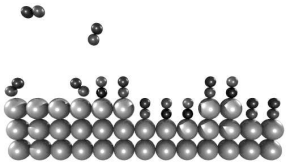

$$\frac{d\vartheta_N}{dt} = -2k_4\vartheta_N^2 - k_6\vartheta_{NO}\vartheta_N + k_3\vartheta_{NO}(1-\vartheta_{CO}-\vartheta_{NO}) = 0$$

$$\frac{d\vartheta_{N_2O}}{dt} = k_6\vartheta_{NO}\vartheta_N - k_7\vartheta_{N_2O} - k_8\vartheta_{N_2O} \qquad = 0.$$

From this, the expressions for ϑ_N and ϑ_{N_2O} can be derived, in which the quadratic formula has been used to obtain the expression for ϑ_N,

$$\vartheta_N = -\frac{1}{4k_4}\left(k_6\vartheta_{NO} \pm \sqrt{k_6^2\vartheta_{NO}^2 + 8k_4k_3\vartheta_{NO}(1-\vartheta_{CO}-\vartheta_{NO})}\right)$$

$$\vartheta_{N_2O} = \frac{k_6\vartheta_{N_2O}\vartheta_N}{k_7+k_8}.$$

Since $\vartheta_N > 0$, the square root term has to be larger than $k_6\vartheta_{NO}$, which means that only the minus solution is valid. Substituting these expressions in equation 3.5.2, and simplifying the outcome, yields

$$\begin{aligned} R_{N_2} = \quad & \frac{-k_7/(k_7+k_8) \;+\; 1/2}{4k_4}\left[k_6^2\vartheta_{NO}^2\right. \\ & -\;\; \left. k_6\vartheta_{NO}\sqrt{k_6^2\vartheta_{NO}^2 + 8k_4k_3\vartheta_{NO}(1-\vartheta_{CO}-\vartheta_{NO})}\right] \\ & +\;\; 1/2\; k_3(1-\vartheta_{CO}-\vartheta_{NO}), \end{aligned}$$

which, after substituting expressions 3.5.4 and 3.5.5, and simplifying, yields equation 3.2.2:

$$\begin{aligned} R_{N_2} = \quad & \frac{k_2 p_{NO}}{4k_{-2}k_4\left(1+\frac{k_1}{k_{-1}}p_{CO}+\frac{k_2}{k_{-2}}p_{NO}\right)^2} \\ & \times \;\; \left[\left(\frac{1}{2}-\frac{k_8}{k_7+k_8}\right)k_6^2\frac{k_2}{k_{-2}}p_{NO}\right. \\ & -\;\; \left.\left(\frac{1}{2}-\frac{k_8}{k_7+k_8}\right)k_6\sqrt{1+\frac{8k_4k_3k_{-2}}{k_6^2k_2p_{NO}}}\;\right] \\ & +\;\; \frac{k_3k_2p_{NO}}{2k_{-2}\left(1-\frac{k_1}{k_{-1}}p_{CO}+\frac{k_2}{k_{-1}}p_{NO}\right)^2}. \end{aligned}$$

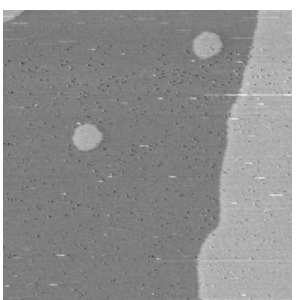

If k_4 is dominant,

$$\lim_{k_4 \to \infty} R_{N_2} = \frac{k_3}{2} \frac{k_2}{k_{-2}} \frac{p_{NO}}{\left(1 + \frac{k_1}{k_{-1}} p_{CO} + \frac{k_2}{k_{-2}} p_{NO}\right)^2},$$

is obtained, and if k_4 is negligible,

$$\lim_{k_4 \to 0} R_{N_2} = \frac{k_3 k_8}{k_7 + k_8} \frac{k_2}{k_{-2}} \frac{p_{NO}}{\left(1 + \frac{k_1}{k_{-1}} p_{CO} + \frac{k_2}{k_{-2}} p_{NO}\right)^2},$$

is obtained, in which $(\sqrt{1+\epsilon})$ is approached by $(1 + 1/2\epsilon)$. The combination of the two limits is exactly equation 3.2.3.